

Electronic and transport properties of Li-doped NiO epitaxial thin films

J. Y. Zhang¹, W.W. Li², R. L. Z. Hoye², J. L. MacManus-Driscoll², M. Budde³, O. Bierwagen³, L. Wang⁴, Y. Du⁴, M. J. Wahila⁵, L. F.J. Piper⁵, T.-L. Lee⁶, H. J. Edwards⁷, V. R. Dhanak⁷, K. H. L. Zhang^{1,2*}

¹*Department of Chemical and Biochemical Engineering, College of Chemistry and Chemical Engineering, Xiamen University, Xiamen 361005, P.R. China*

²*Department of Materials Science & Metallurgy, University of Cambridge, 27 Charles Babbage Road, Cambridge, CB3 0FS, United Kingdom*

³*Paul-Drude-Institut für Festkörperelektronik, Hausvogteiplatz 5-7, DE-10117 Berlin, Germany*

⁴*Physical Sciences Division, Physical & Computational Sciences Directorate, Pacific Northwest National Laboratory, Richland, Washington 99352, USA*

⁵*Materials Science & Engineering, Binghamton University, Binghamton, New York 13902, USA*

⁶*Diamond Light Source Ltd., Harwell Science and Innovation Campus, Didcot, OX11 0DE, United Kingdom*

⁷*Department of Physics, University of Liverpool, Liverpool L69 3BX, United Kingdom*

Email: kelvinzhang@xmu.edu.cn

Abstract:

NiO is a p-type wide bandgap semiconductor of use in various electronic devices ranging from solar cells to transparent transistors. Understanding and improving its optical and transport properties have been of considerable interest. In this work, we have investigated the effect of Li doping on the electronic, optical and transport properties of NiO epitaxial thin films grown by pulsed laser deposition. We show that Li doping significantly increases the p-type conductivity of NiO, but all the films have relatively low room-temperature mobilities ($< 0.05 \text{ cm}^2 \text{ V}^{-1} \text{ s}^{-1}$). The conduction mechanism is better described by small-polaron hopping model in the temperature range of $200 \text{ K} < T < 330 \text{ K}$, and variable range hopping at $T < 200 \text{ K}$. A combination of x-ray photoemission and O K-edge x-ray absorption spectroscopic investigations reveal that the Fermi level gradually shifts toward the valence band maximum (VBM) and a new hole state develops with Li doping. Both the VBM and hole states are composed of primarily Zhang-Rice bound states, which accounts for the small polaron character (low mobility) of hole conduction. Our work provides guidelines for the search for p-type oxide materials and device optimization.

Keywords: oxide semiconductor; hole transport layer; NiO; Transparent conducting oxides

1. Introduction

Transparent oxide semiconductors (TOS) constitute a class of materials that uniquely combine the properties of electrical conductivity and optical transparency.^{1, 2} TOS are needed for a wide range of electronic and optoelectronic applications including solar cells, flat panel displays, light emitting diodes, photodetectors and transparent electronics.³⁻⁷ Most of the industry standard TOS are n-type wide bandgap oxides ($E_g > 3.1$ eV), such as In_2O_3 , SnO_2 and ZnO , whose conductivity can be further tuned by aliovalent doping or formation of oxygen vacancies.^{6, 8-10} In contrast, the development of p-type TOS remains a grand material challenge.^{11, 12} This difficulty is thought to be due to the localized nature of the O 2p-derived valence band (VB) which leads to difficulty in introducing shallow acceptors and large hole effective masses. In 1997, Hosono and co-workers proposed the concept of “chemical modulation of the valence band” to mitigate this problem using hybridization of O 2p orbitals with closed-shell Cu 3d¹⁰ orbitals.¹³ This work has triggered a flurry of efforts to design efficient p-type TOS and understand their fundamental materials properties, including a series of Cu⁺-based delafossites,¹⁴⁻¹⁶ nd^6 spinel oxides,¹⁷⁻¹⁹ Cr³⁺-based oxides (3d³)^{20, 21} and post-transition metal oxides with filled lone pair state (ns^2).²²⁻²⁴ However, these oxides still suffer from issues such as low carrier mobilities, low visible light transparency or chemical instability.^{12, 25}

NiO is actually the first known p-type TOS.^{12, 26-28} It has been widely used as a p-type channel material in ultraviolet (UV) photodetectors and transparent field-effect transistors,^{29, 30} and as hole-transporting layers (HTL) in organic solar cells^{31, 32} and light emitting diodes^{33, 34}. For example, Ohta *et al.* have fabricated transparent epitaxial NiO/ZnO p-n heterojunctions, where the diode shows a high responsivity for UV light detection.²⁹ With recent booming development of hybrid organic-inorganic perovskite solar cells, NiO has been extensively explored as a HTL to replace the highly corrosive PEDOT:PSS layer, due to its high stability, ease of scalability and deep-lying VB that matches well with the VB of $\text{CH}_3\text{NH}_3\text{PbI}_3$.³² Breakthroughs have been made by using Li and Mg co-doped NiO to increase the electrical conductivity, leading to efficient and stable large-area perovskite solar cells with an excellent fill factor.³⁵ For all these applications, the electrical and optical properties

of the NiO layers as well as their interfacial energy levels with respect to other materials play an important role in determining the device performance.

NiO crystallizes in a rock-salt crystal structure, in which Ni cations have a nominal valence state of +2 ($3d^8$) in octahedral coordination (see Figure 1a and b). Due to a strong electron correlation in 3d orbitals, it has an optical bandgap of 3.4-4.0 eV. The energy level of Ni 3d is close to that of an O $2p^6$ level. It is expected that the Ni 3d orbitals can hybridize strongly with O $2p^6$ orbitals, in a similar way as the electronic structures in Cu^+ -based delafossites. Stoichiometric NiO should be very insulating. The intrinsic p-type conductivity is attributed to hole states induced by Ni vacancies (nominally $Ni_{1-x}O$) formed in oxygen-rich conditions. Enhanced conductivity can also be achieved in a more controlled way by replacing Ni^{2+} cations with monovalent cations such as Li^+ . Each Li^+ ion in principle donates one hole into the top of VB in order to keep charge neutrality.³⁶⁻³⁸ However, there is uncertainty in the literature regarding the hole mobility and conduction mechanism.^{27, 39-41} Two different models have been suggested for the conduction mechanism: (i) conventional band-like conduction, or (ii) small polaron hopping (SPH) in which the carriers interact strongly with its surrounding lattice to form heavy quasiparticles called polarons; the polaron conduction occurs through thermally activated hopping from one site to another. High *p*-type mobilities have been reported in polycrystalline NiO thin films deposited by magnetron sputtering ($28.99 \text{ cm}^2 \text{ V}^{-1} \text{ s}^{-1}$)⁴², thermal oxidization ($5.2 \text{ cm}^2 \text{ V}^{-1} \text{ s}^{-1}$)⁴³, spray-pyrolysis ($11.96 \text{ cm}^2 \text{ V}^{-1} \text{ s}^{-1}$)⁴⁴ and sol-gel spin coating ($25 \text{ cm}^2 \text{ V}^{-1} \text{ s}^{-1}$)⁴⁵. These values are comparable with those of *n*-type TOS and would hold great promise for many device applications. On the other hand, many other experimental studies have suggested NiO exhibits rather low hole mobilities ($< 0.1 \text{ cm}^2 \text{ V}^{-1} \text{ s}^{-1}$) due to the localized nature of the VB arising from strong electron correlation.^{27, 41, 46} For those reports, the conduction mechanism is better described by a SPH model. It should be noted that most of the previous experiments were performed on polycrystalline powders/films, where results are likely to be influenced by grain boundaries and other defects.

Motivated by the promise of NiO in various device applications and to answer the aforementioned fundamental questions, the goal of this work is to carry out a detailed

investigation of the electronic, optical and transport properties of structurally well-defined Li doped NiO epitaxial thin films. To this end, we have grown Li doped NiO ($\text{Li}_x\text{Ni}_{1-x}\text{O}$ with $x=0, 0.006, 0.03, 0.06$ and 0.09) films on $\text{MgO}(001)$ substrates by pulsed laser deposition (PLD). Compared with polycrystalline powders/thin films in previous studies, the use of high-quality epitaxial thin films with a considerably reduced number of grain boundaries and associated defects, should reveal more intrinsic materials properties. The evolution of electronic, optical and transport properties of $\text{Li}_{1-x}\text{Ni}_x\text{O}$ with x was investigated by a combination of X-ray photoemission spectroscopy (XPS), X-ray absorption spectroscopy (XAS), transport measurement, Seebeck measurement, and optical absorption spectra studies. We show that Li doping significantly increases the p-type conductivity of NiO, but all the films have relatively low room-temperature mobilities ($< 0.05 \text{ cm}^2 \text{ V}^{-1}\text{s}^{-1}$). The conduction mechanism is better described with SPH model in the temperature range of $200 \text{ K} < T < 330 \text{ K}$, and variable range hopping for $T < 200 \text{ K}$. The combined XPS and O K-edge XAS spectra reveal that the Fermi level (E_f) gradually shifts toward the valence band maximum (VBM) with Li doping and a new hole state develops above the E_f . Both the VBM and hole states are of primarily Zhang-Rice bound states, consistent with hole conduction by SPH.

2. Experimental details

Epitaxial $\text{Li}_x\text{Ni}_{1-x}\text{O}$ thin films with $x=0, 0.006, 0.03, 0.06$ and 0.09 were grown on double-side polished (001)-oriented MgO substrates by PLD from respective targets. The targets were prepared by mixing and grinding the appropriate proportions of Li_2CO_3 and NiO. The powder was heated at 650°C for 8 hours in air, and then pelletized and heated again at 850°C for 12 hours. Laser ablation was performed at a repetition rate of 5 Hz and an energy density of 1.0 J/cm^2 with a 248 nm KrF excimer. Films with thicknesses ranging from 20 to 30 nm were grown at a substrate temperature of 500°C in 0.1 Torr oxygen partial pressure, and cooled to room temperature in 1 Torr O_2 . One undoped NiO film was grown on 0.1% Nb doped SrTiO_3 (001) in order to avoid charging effect for XPS measurements. The crystal structure and epitaxial relationship in the films were determined by high-resolution XRD using a PANalytical four-circle diffractometer in θ - 2θ scans and reciprocal space mapping (RSM) modes. Optical absorption measurements were performed at room temperature using a

Cary 5000 spectrophotometer in the photon energy range of 0.5–3.5 eV. Electrical resistivity measurements were performed using van der Pauw method with Ag contacts in the temperature range of 130–330 K.

High-resolution XPS using a monochromatic Al $K\alpha_1$ x-ray ($h\nu = 1486.6$ eV) source was carried out at normal emission (electron take-off angle = 90° relative to the surface plane) with a SPECS PHOIBOS 150 electron energy analyzer. The total energy resolution was about 0.50 eV, limited by the source. The binding energy (BE) was calibrated using a polycrystalline Au foil placed in electrical contact with the film surface after deposition, which simultaneously helped avoid charging effects during XPS measurements.

Workfunction measurements were determined in a separate UHV system consisting of a monochromated Al $K\alpha_1$ x-ray source together with a five channeltron PSP electron energy analyzer. The PSP spectrometer was calibrated using a clean silver foil and the measurements made at an overall resolution of 0.3 eV. The workfunction was determined by measuring the XPS secondary electron cut-off with the sample at a bias voltage of -10 V. The overall precision of the measurement was ± 0.05 eV. XAS were measured in total electron yield (TEY) mode at beamline I09 Diamond Light Source (DLS) by measuring the sample drain current. The energy resolution was set at 0.1 eV for the O K edge. The energy scale of the XAS measurements was calibrated using first- and second-order diffraction Ti $L_{3,2}$ -edge absorption features of a single crystal rutile TiO_2 reference.

3. Results and discussion

3.1 Thin Film Growth

Both bulk NiO and MgO adopt the same rocksalt crystal structure with different lattice parameters of $a_{\text{NiO}} = 4.177$ Å and $a_{\text{MgO}} = 4.212$ Å (Figure 1a), which result in a little lattice mismatch of 0.8%. The deposition of Li doped NiO on MgO is expected to behave very similarly to that of pure NiO, except for a slight increase in lattice mismatch because of shrinkage of lattice parameters upon Li doping. XRD θ - 2θ out-of-plane scans (Figure 1c) show the (002) reflections of $\text{Li}_x\text{Ni}_{1-x}\text{O}$ films with well-defined Kiessig fringes close to MgO (002) reflection, confirming the planar character of the surfaces and interfaces and the high quality of the

epitaxial films. The increase in film (002) Bragg angle in XRD with Li doping reveals a systematic reduction of out-of-plane lattice constant. To gain additional structural information, RSMs near the (113) reflection of MgO were measured. The in-plane and out-of-plane lattice parameters of the films as a function of Li doping concentration were extracted from RSMs and are shown in Figure 1d. The in-plane lattice parameters for different x are nearly the same as that of MgO, indicating all the films are coherently strained by the substrates. Since Li^+ cations in octahedral coordination have a slightly larger ionic radius (0.90 Å) than that of Ni^{2+} (0.83 Å), the reduction of the lattice constant for $\text{Li}_x\text{Ni}_{1-x}\text{O}$ is most likely due to the smaller size of Ni^{3+} cations (0.70 Å) associated with hole doping.²⁸

3.2 Electrical and optical properties

The transport properties of the $\text{Li}_x\text{Ni}_{1-x}\text{O}$ film series were measured using the van der Pauw method in the temperature range of 130-330 K. Pure NiO is not sufficiently conductive to be measurable ($\sigma < 10^{-4}$ S/cm), indicating no significant density of electrically active defects, i.e., Ni vacancies (V_{Ni}). With Li doping, the conductivity (σ) increases rapidly. The room-temperature (RT) conductivities ranges from ~0.1 S/cm at $x = 0.006$ to 11.2 S/cm at $x = 0.09$ and all values are given in Table I. The RT conductivities of the epitaxial films are much higher than those for polycrystalline thin films at comparable Li doping levels.^{26, 27} This difference suggests that grain boundaries and electrically active defects and/or impurities play an influential role in determining transport properties in polycrystalline films. Repetitive measurements were made to measure the carrier concentration (p) and mobility (μ) using Hall effect measurement. However, it was not possible to extract a reliable Hall coefficient. This is possibly due to the mobility being below the upper limit of our Hall setup ($\mu \approx 0.1 \text{ cm}^2 \text{ V}^{-1} \text{ s}^{-1}$). If the mobility lies below the Bosman and Van Daal limit ($\mu < 0.1 \text{ cm}^2 \text{ V}^{-1} \text{ s}^{-1}$), it is likely that the hole conduction mechanism follows the SPH model.⁴¹ SPH has been observed in many mixed-valence transition metal oxides such as Cr_2O_3 ,⁴⁷ Fe_2O_3 ,⁴⁸ CoO ,⁴¹ and p-type TOSs such as CuCrO_2 ⁴⁹ and LaCrO_3 .²⁰ Small polarons conduct by thermally activated hopping of carriers from one site to another. The relationship between conductivity and temperature is given by $\sigma(T) = (\sigma_0/T) \exp(E_a/k_B T)$, where E_a is the activation energy for hopping and k_B is the Boltzmann constant. Figure 2a plot the fit of temperature dependent conductivity data to a SPH model: In

($\sigma \cdot T$) vs ($1/T$). It can be seen that the data fit well with SPH in temperature range of 220-330 K. The E_a determined from the slopes of the fit lines decreases from 0.224 eV to 0.166 eV (Table I). Below 220 K, the conduction data deviates from the SPH model, but fits well with variable-range hopping (VRH) which has a $T^{-1/4}$ temperature dependence (Figure 2b).

In order to determine the p and μ , we measured the Seebeck coefficients, S , as described in detail in the literature.⁵⁰ All films exhibit positive S values decreasing from +649 to +239 $\mu\text{V/K}$ from $x = 0.006$ to 0.09, confirming p -type conductivity (see Figure 2c and Table 1). The Seebeck coefficient can be used as a direct measure of the fraction of hopping sites occupied with holes, c , based on formula: $S(c) = (k_B/e) \ln[2(1-c)/c]$, where e is the elementary electronic charge e . Hole creation by Li doping at a Ni site thus corresponds to activation of an adjacent Ni site for hole hopping, i.e. $p(c) = cN_{\text{Ni}}$, where $p(c)$ is the hole carrier concentration and N_{Ni} is the Ni number density, $5.5 \times 10^{22} \text{ cm}^{-3}$. Based on the formulae for $S(c)$ and $p(c)$, we determined the hole concentration to range from $5.90 \times 10^{19} \text{ cm}^{-3}$ to $6.13 \times 10^{21} \text{ cm}^{-3}$. The corresponding mobilities at RT (determined from $\sigma = e\mu p$) are in the range from 0.011 to 0.047 $\text{cm}^2 \text{ V}^{-1} \text{ s}^{-1}$ (see Table I). The mobilities from our epitaxial thin films are consistent with values in ref [26,27], but much lower than in ref [42-45]. Nonetheless, Li doped NiO is still a promising candidate for device applications that are not adversely affected by low mobility, such as rectifiers, photodetectors, and n-type junction field-effect transistors. Very recently, Liu *et al.* have demonstrated that doping of Cu in NiO could introduce more dispersion at the top of valence band, and thus is an effective strategy to improve the mobility of NiO thin films for transparent electronics.⁵¹

Taking c from the Seebeck analysis, we also modeled the RT SPH-conductivity, $\sigma_{\text{SPH}} = g\nu Ne^2 a^2 c(1-c) \exp(-E_a/k_B T)/k_B T$,^[44] with geometric factor g (on the order of unity), optical phonon of frequency ν and nearest neighbor distance between Ni hopping sites $a = 4.177 \text{ \AA}$. We found $\nu = 9.7 \times 10^{12} \text{ Hz}$ to yield the best fit of the SPH model to our measured RT conductivity. The overall agreement between hole concentration and conductivity calculated from SPH and Li-concentration and measured conductivity further supports SPH-related transport.

Figure 3a and b shows optical transmission and absorption spectra for the films with x . Table I also summarizes the averaged transmission at wavelengths of 420, 490, 560, 630 and 700 nm. Pure NiO and $x = 0.006$ films show very high transparency ($T > 81\%$), because of the large optical bandgap of NiO (3.65 eV as determined from our measurement). Li doping induces two broad absorption features centered at ~ 1.1 eV and 2.2 eV, resulting in slight black coloration in the films. Our results suggest that $x = 0.006$ films fulfill the optical transparency and conductivity requirements to be used as an effective HTL materials in photovoltaic cells.

3.3 Electronic Structures

To elucidate the optical and transport properties, we performed detailed characterizations on the electronic structures of $\text{Li}_x\text{Ni}_{1-x}\text{O}$ using combined XPS and XAS. Figure 4 a and b show XPS core levels of O 1s and Ni $2p_{3/2}$, respectively. All XPS spectra are referenced to the E_f as zero. The E_f was calibrated using a polycrystalline Au foil placed in electrical contact with the film surfaces. There is a parallel shift of the BEs of O 1s and Ni $2p_{3/2}$ toward lower values with increasing x . The shift of BEs is consistent with the overall picture of downward movement of E_f in hole doped semiconductors. This trend has also been observed in many hole-doped transition metal oxides, such as Sr doped LaBO_3 ($B=\text{Ti, Cr, Mn, Fe}$) and $\text{La}_{2-x}\text{Sr}_x\text{CuO}_4$.⁵²⁻⁵⁴ We thus take the average shift of the BEs as a measure of shift of E_f ($\Delta\mu$), as shown in Figure 5a. Figure 4c show the VB spectra of the $\text{Li}_x\text{Ni}_{1-x}\text{O}$ films. The spectrum for NiO is very similar to the ones reported earlier in the literature and it shows the characteristic feature “A” close to the E_f , a satellite “B” at ~ 3.5 eV and broad feature “C” in the region of 4-11 eV.³⁶ The VBM for NiO is determined to be 0.7 ± 0.1 eV below E_f by linear extrapolation of the leading edge of the VB to zero baseline intensity. The VBM position further confirms the intrinsic p-type character of NiO. Li doping introduces hole states at the top VB and gradually shifts the VBM toward E_f . As shown in Figure 5a, the shift of VBM to E_f is in agreement with the shift of E_f determined by core levels. The downward movement of E_f also parallels the increase in RT conductivity with x .

We also measured the workfunctions (Φ_w) as a function of Li doping using XPS by determining the difference between the width of the photoemission spectrum and the source energy (Figure 5b). The onset of secondary emission was determined by a linear extrapolation of the cutoff edge to the zero baseline intensity. The Φ_w for NiO is determined to be ~ 4.85 eV. This is a reasonable value, considering the ionization potential (IP) for NiO is 5.40 eV and the VBM is 0.7 eV below E_f ($IP = \Phi_w + VBM$). This value is in agreement with recent report for NiO films grown by solution processing on ITO without plasma treatment,⁵⁵ but is less than the value (5.3 eV) previously reported for NiO films treated in oxygen plasma.⁵⁶ The work function of a material is affected by two independent qualities: (i) the Fermi level position; and (ii) the surface dipole.⁵⁷ It is likely that oxygen plasma may result in a large upward band bending and thus a larger Φ_w due to the formation of electronegative species, e.g., O^- or NiOOH groups. The Φ_w for Li doped NiO increased to 4.95 eV for $x=0.006$ and 5.04 eV for $x=0.06$, due to the downward shift of the E_f . However, the amount of increase is less than the $\Delta\mu$. This indicates Li dopants in our films might introduce electropositive absorbates which lower the Φ_w . Nonetheless, the enhanced conductivity and increased workfunctions through Li doping is of particular interest for use of Li doped NiO as a hole transport layer in solar cells, where the shunt resistance should be lowered and interface band alignment optimized.^{35, 58} For example, we have recently shown that bismuth oxyiodide (BiOI) is a promising air-stable photovoltaic materials beyond halide perovskites, but its efficiency is still limited below 1.8%.⁵⁹ These compounds have a higher work function and ionisation potential than conventional absorbers because the Bi 6s orbitals have a deep energy level. A workfunction would need to be increased above 5.1 eV in order to avoid downwards band-bending at the HTL interface. This downwards band-bending restricts the short circuit current and fill factors, as well as limiting the open-circuit voltage by limiting quasi-Fermi level splitting.

Figure 6a shows the O K-edge XAS spectra. The O K-edge XAS probes the transition from O 1s to unoccupied states with partial O 2p character hybridized with Ni 3d states. The spectra can be qualitatively related to the unoccupied density of states above the E_f .^{59, 60} The O K-edge XAS for pure NiO shown in Figure 6a agrees well with data reported in the literature.^{36,}

⁶⁰ The feature at 532 eV (marked as D) is attributed to the unoccupied Ni 3d e_g hybridized

with O 2p orbitals, forming the bottom of the CB; the other higher energy features (marked as E) at 534-541 eV correspond to transitions to the Ni 4s and 4p states hybridized with O 2p. A new unoccupied state gradually increases at 529 eV with Li concentration, which can be assigned to be the hole state (acceptor state) induced by Li doping. A sketch for this energy level diagram is shown in Figure 6b. Therefore, the two broad absorption features at ~ 1.1 eV (“ α ”) and 2.2 eV (“ β ”) in the optical absorption spectra shown in Figure 3b can be assigned to optical excitation from VB to the hole state, resulting in the increase in black coloration with x. It is also expected that this hole state may produce important effects on device transport characteristics, *e.g.*, acting as recombination centers or traps for free carriers in p-n diodes leading to a large leakage current at reverse bias.

It is interesting to consider the nature of the hole state. For a long time, NiO was thought to be a prototypical Mott insulator in which the insulating gap is caused by on-site Coulomb energy, *i.e.*, both the top of VB and bottom of CB are of Ni 3d character. Later, Sawatzky *et al.* re-defined NiO as a charge-transfer (CT) insulator, in which the insulating gap is formed between the O 2p and the empty Ni 3d.⁶⁰ This picture indicated the top of the VB spectra is of mainly $3d^8\bar{L}$ character, where \bar{L} denotes a hole in the O 2p ligand state. However, very recently it was proved by Taguchi *et al.* that the feature A in VB is better described as Zhang-Rice (ZR) doublet bound states.⁶¹ The ZR doublet bound states originate from the strong hybridization between O 2p–Ni 3d and the Ni on-site Coulomb interaction. This result strongly suggests that hole states responsible for transport properties are of primarily ZR character. The narrow bandwidth of the ZR states dictate the polaronic nature of hole conduction with the very limited mobility.

Lastly, returning to Fig. 4b and d, the Ni 2p_{3/2} shows a complicated line shape consisting of a main peak (a), shoulder (b), and satellite structure (c). The Ni 2p_{3/2} spectra for different x were normalized with respect to the peak height at the feature c. According to the recent ZR bound state model, features a, b and c are mainly attributed to final states of well screened $2p^53d^9Z$, $2p^53d^9\bar{L}$, and poorly screened $2p^53d^8$ final states, respectively, where Z denotes a hole in the ZR doublet bound states and \bar{L} a hole in the O 2p ligand states. With Li doping, there is a slight decrease of the intensity ratio of a/b. This is caused by the reduction of ZR states at the VBM

by hole doping. The slight change of a/b ratio can be used as an indication for hole states in NiO. However, we note many reports^{32, 62, 63} fit peaks a and b into two singlets and attribute a and b as Ni^{2+} and Ni^{3+} , respectively. This would lead to an inaccurate explanation of electronic properties of NiO and overestimation of hole carrier concentrations.

4. Conclusions

In summary, we have investigated the effect of Li doping on the electronic, optical and transport properties of NiO epitaxial thin films grown by PLD. We show that Li doping significantly increases the p-type conductivity of NiO. The conduction mechanism is better described with a SPH model in the temperature range of $200\text{ K} < T < 330\text{ K}$, and variable range hopping at $T < 200\text{ K}$. XPS reveals that the E_f gradually shifts toward the VBM with Li doping, while XAS shows the development of a new hole state above the E_f . Both the VBM and the hole states are composed of primarily ZR bound states, consistent with the conduction of holes by SPH. Li doped NiO could be of promising use as a hole transport layer for solar cells. The increase in work function and conductivity could improve the device's fill factor, short-circuit current density and open-circuit voltage. On the other hand, the low mobility would suggest a short hole diffusion length. This issue could be solved by limiting the thickness of the Li-doped NiO layer, or modifying the dispersion at the VB by doping, e.g., Cu doping.⁵¹

Acknowledgments

K.H.L. Zhang is grateful for funding support by the Thousand Youth Talents Program of China and Herchel Smith Postdoctoral Fellowship by University of Cambridge. J. L. MacManus-Driscoll, R. Hoyer and W. Li acknowledge support from EPSRC grants EP/L011700/1, EP/N004272/1, and EP/P027031. The contribution of MB and OB was performed in part in the framework of GraFOx, a Leibniz-ScienceCampus partially funded by the Leibniz association. M.B. gratefully acknowledges financial support by the Leibniz Association. We thank Diamond Light Source for access to beamline I09 (SI 16005), which contributed to the results presented here. We also thank beamline scientist Christoph Schlueter at Diamond Light Source for their assistance.

Contribution of the co-authors

J. Y. Zhang analyzed experimental data and wrote the manuscript. K. H. L. Zhang lead this work and grew the samples. W.W. Li, R. L. Z. Hoye and J. L. MacManus-Driscoll performed the XPS measurements; M. Budde and O. Bierwagen carried out Seebeck measurement. L. Wang and Y. Du carried out resistivity measurement. M. J. Wahila, L. F.J. Piper and T.-L. Lee performed X-ray absorption at Diamond Synchrotron. H. J. Edwards and V. R. Dhanak performed workfunction measurements. All the authors help to improve the manuscript.

Table I. Film thickness (d), room-temperature conductivities (σ), activation energies (E_a) for small polaron hopping, Seebeck coefficients (S), extracted hole concentration (p) and mobility (μ), and wavelength-averaged transmissions (T) for $\text{Li}_x\text{Ni}_{1-x}\text{O}$ on $\text{MgO}(001)$.

x	d	σ	E_a	S	p	μ	T
	[nm]	[S cm ⁻¹]	[eV]	[$\mu\text{V K}^{-1}$]	[cm ⁻³]	[cm ² V ⁻¹ s ⁻¹]	[%]
0	31	NA	NA	NA	NA	NA	87.3
0.006	32	0.10	0.224	649	5.90×10^{19}	0.011	80.9
0.03	31	2.7	0.185	485	3.94×10^{20}	0.047	66.6
0.06	29	6.6	0.182	297	3.31×10^{21}	0.023	54.9
0.09	19	11.2	0.166	239	6.13×10^{21}	0.025	44

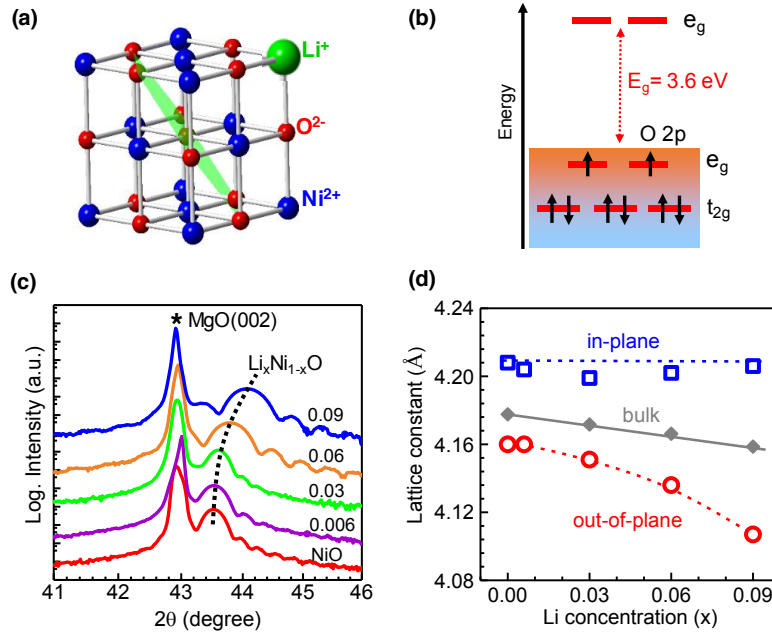


Figure 1. Epitaxial growth of $\text{Li}_x\text{Ni}_{1-x}\text{O}$ thin films on $\text{MgO}(001)$. (a) Crystal structure of NiO doped with Li at Ni site; (b) schematic diagram of electronic structure of NiO; (c) x-ray diffraction in the vicinity of the MgO (002) reflection; (d) change of the in-plane and out-of-plane lattice parameters as function of Li doping level extracted from respective RSMs. the bulk lattice parameters are measured from polycrystalline targets.

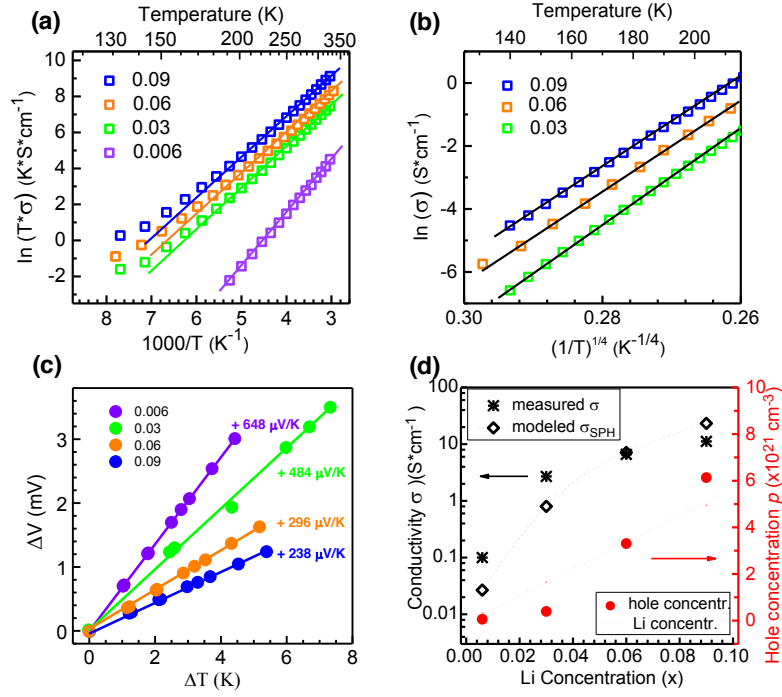


Figure 2. Electrical and thermoelectric properties. (a) Plots of temperature dependent conductivity data in the small polaron model: $\ln(\sigma^*T)$ vs $(1/T)$; (b) Fits of the data to variable range hopping from 130 K to 210 K: $\ln(\sigma)$ vs $(1/T)^{1/4}$; (c) Seebeck measurements, showing p-type carriers; (d) The combination of Seebeck and Conductivity to get mobility and carrier concentrations

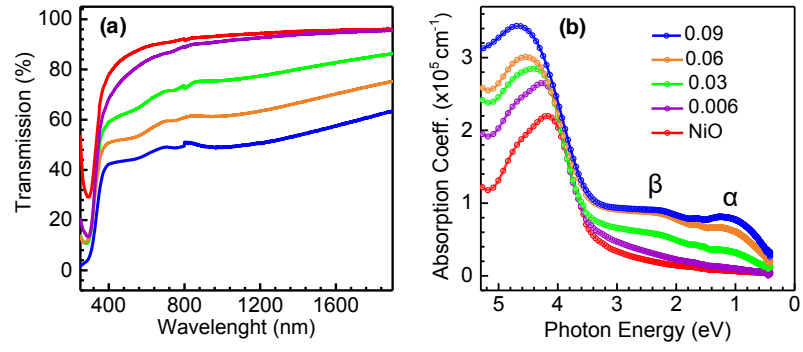


Figure 3. (a) optical transmission of the films; (b) optical absorption coefficient as a function of photon energy.

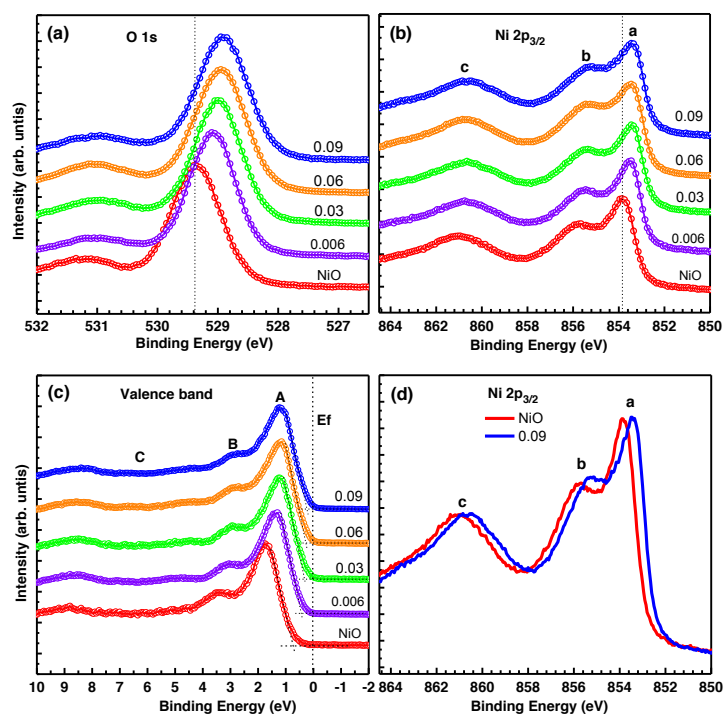


Figure 4. (a) O 1s, (b) Ni 2p_{3/2}, (c) valence band spectra for $\text{Li}_x\text{Ni}_{1-x}\text{O}$ with different x ; and (d) a detailed comparison for Ni 2p_{3/2} from NiO and 0.09.

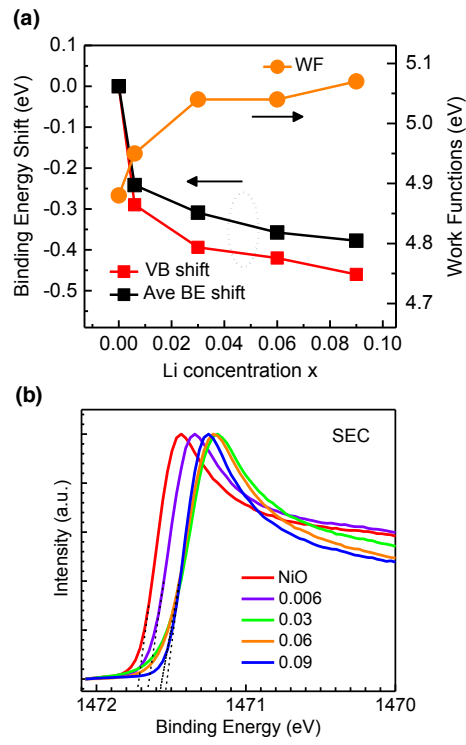


Figure 5. (a) Average chemical potential shift ($\Delta\mu$) deduced from the change of O 1s and Ni 2p_{3/2} binding energies, VBM shift and work function vs. x ; (b) Secondary energy cutoff used to calculate the work function of Li doping.

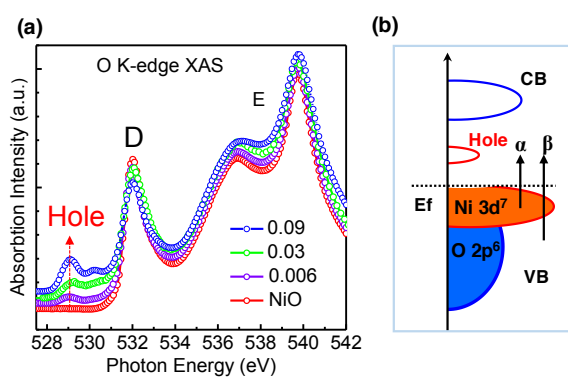


Figure 6. (a) O K-edge XAS spectra for $\text{Li}_x\text{Ni}_{1-x}\text{O}$ films; (b) Schematic energy diagram for Li doped NiO.

Reference:

1. P. P. Edwards, A. Porch, M. O. Jones, D. V. Morgan and R. M. Perks, *Dalton Transactions*, 2004, 2995.
2. K. Ellmer, *Nature Photonics*, 2012, **6**, 808.
3. X. G. Yu, T. J. Marks and A. Facchetti, *Nat. Mater.*, 2016, **15**, 383.
4. C. G. Granqvist, *Solar Energy Materials and Solar Cells*, 2007, **91**, 1529.
5. E. Fortunato, D. Ginley, H. Hosono and D. C. Paine, *Mrs Bulletin*, 2007, **32**, 242.
6. T. Minami, *Semiconductor Science and Technology*, 2005, **20**, S35.
7. K. Nomura, H. Ohta, K. Ueda, T. Kamiya, M. Hirano and H. Hosono, *Science*, 2003, **300**, 1269.
8. G. J. Exarhos and X. D. Zhou, *Thin Solid Films*, 2007, **515**, 7025.
9. K. H. L. Zhang, R. G. Egdell, F. Offi, S. Iacobucci, L. Petaccia, S. Gorovikov and P. D. C. King, *Physical Review Letters*, 2013, **110**, 056803.
10. S. C. Dixon, D. O. Scanlon, C. J. Carmalt and I. P. Parkin, *Journal Of Materials Chemistry C*, 2016, **4**, 6946.
11. G. Hautier, A. Miglio, G. Ceder, G. M. Rignanese and X. Gonze, *Nat. Commun.*, 2013, **4**, 2292.
12. K. H. L. Zhang, K. Xi, M. G. Blamire and R. G. Egdell, *J. Phys.-Condes. Matter*, 2016, **28**, 383002.
13. H. Kawazoe, M. Yasukawa, H. Hyodo, M. Kurita, H. Yanagi and H. Hosono, *Nature*, 1997, **389**, 939.
14. H. Kawazoe, H. Yanagi, K. Ueda and H. Hosono, *Mrs Bulletin*, 2000, **25**, 28.
15. M. K. Jayaraj, A. D. Draeseke, J. Tate and A. W. Sleight, *Thin Solid Films*, 2001, **397**, 244.
16. R. Nagarajan, A. D. Draeseke, A. W. Sleight and J. Tate, *Journal of Applied Physics*, 2001, **89**, 8022.
17. S. Narushima, H. Mizoguchi, K. Shimizu, K. Ueda, H. Ohta, M. Hirano, T. Kamiya and H. Hosono, *Adv. Mater.*, 2003, **15**, 1409.
18. M. Dekkers, G. Rijnders and D. H. A. Blank, *Applied Physics Letters*, 2007, **90**, 021903.
19. F. L. Schein, M. Winter, T. Bontgen, H. von Wenckstern and M. Grundmann, *Applied Physics Letters*, 2014, **104**, 022104.
20. K. H. L. Zhang, Y. G. Du, A. Papadogianni, O. Bierwagen, S. Sallis, L. F. J. Piper, M. E. Bowden, V. Shutthanandan, P. V. Sushko and S. A. Chambers, *Adv. Mater.*, 2015, **27**, 5191.
21. A. B. Kehoe, E. Arca, D. O. Scanlon, I. V. Shvets and G. W. Watson, *J. Phys.-Condes. Matter*, 2016, **28**, 125501.
22. Y. Ogo, H. Hiramatsu, K. Nomura, H. Yanagi, T. Kamiya, M. Hirano and H. Hosono, *Applied Physics Letters*, 2008, **93**, 032113.
23. A. Bhatia, G. Hautier, T. Nilgianskul, A. Miglio, J. Y. Sun, H. J. Kim, K. H. Kim, S. Chen, G. M. Rignanese, X. Gonze and J. Suntivich, *Chem. Mat.*, 2016, **28**, 30.
24. J. P. Allen, D. O. Scanlon, L. F. J. Piper and G. W. Watson, *Journal Of Materials Chemistry C*, 2013, **1**, 8194.

25. V. A. Ha, F. Ricci, G. M. Rignanes and G. Hautier, *Journal Of Materials Chemistry C*, 2017, **5**, 5772.
26. H. Sato, T. Minami, S. Takata and T. Yamada, *Thin Solid Films*, 1993, **236**, 27.
27. E. Antolini, *Materials Chemistry And Physics*, 2003, **82**, 937.
28. J. B. Goodenough, D. G. Wickham and W. J. Croft, *Journal of Physics and Chemistry of Solids*, 1958, **5**, 107.
29. H. Ohta, M. Hirano, K. Nakahara, H. Maruta, T. Tanabe, M. Kamiya, T. Kamiya and H. Hosono, *Applied Physics Letters*, 2003, **83**, 1029.
30. H. Ohta, M. Kamiya, T. Kamaiya, M. Hirano and H. Hosono, *Thin Solid Films*, 2003, **445**, 317.
31. M. D. Irwin, B. Buchholz, A. W. Hains, R. P. H. Chang and T. J. Marks, *Proceedings Of the National Academy Of Sciences Of the United States Of America*, 2008, **105**, 2783.
32. J. Y. Jeng, K. C. Chen, T. Y. Chiang, P. Y. Lin, T. D. Tsai, Y. C. Chang, T. F. Guo, P. Chen, T. C. Wen and Y. J. Hsu, *Adv. Mater.*, 2014, **26**, 4107.
33. Y. K. Chih, J. C. Wang, R. T. Yang, C. C. Liu, Y. C. Chang, Y. S. Fu, W. C. Lai, P. Chen, T. C. Wen, Y. C. Huang, C. S. Tsao and T. F. Guo, *Adv. Mater.*, 2016, **28**, 8687.
34. J. M. Caruge, J. E. Halpert, V. Bulovic and M. G. Bawendi, *Nano Lett.*, 2006, **6**, 2991.
35. W. Chen, Y. Z. Wu, Y. F. Yue, J. Liu, W. J. Zhang, X. D. Yang, H. Chen, E. B. Bi, I. Ashraful, M. Gratzel and L. Y. Han, *Science*, 2015, **350**, 944.
36. J. Vanelp, H. Eskes, P. Kuiper and G. A. Sawatzky, *Phys. Rev. B*, 1992, **45**, 1612.
37. I. J. Pickering, G. N. George, J. T. Lewandowski and A. J. Jacobson, *J. Am. Chem. Soc.*, 1993, **115**, 4137.
38. H. R. Chen and J. H. Harding, *Phys. Rev. B*, 2012, **85**, 115127.
39. A. J. Bosman and Crevecoe.C, *Physical Review*, 1966, **144**, 763.
40. E. Iguchi and K. Akashi, *J. Phys. Soc. Jpn.*, 1992, **61**, 3385.
41. A. J. Bosman and H. J. Vandaal, *Advances In Physics*, 1970, **19**, 1.
42. S. C. Chen, C. K. We, T. Y. Kuo, W. C. Peng and H. C. Lin, *Thin Solid Films*, 2014, **572**, 51.
43. J. Jiang, X. Wang, Q. Zhang, J. Li and X. X. Zhang, *Phys. Chem. Chem. Phys.*, 2013, **15**, 6875.
44. C. C. Wu and C. F. Yang, *ACS Appl. Mater. Interfaces*, 2013, **5**, 4996.
45. F. K. Shan, A. Liu, H. H. Zhu, W. J. Kong, J. Q. Liu, B. C. Shin, E. Fortunato, R. Martins and G. X. Liu, *Journal Of Materials Chemistry C*, 2016, **4**, 9438.
46. S. Hufner, *Advances In Physics*, 1994, **43**, 183.
47. L. Farrell, K. Fleischer, D. Caffrey, D. Mullarkey, E. Norton and I. V. Shvets, *Phys. Rev. B*, 2015, **91**, 125202.
48. B. Zhao, T. C. Kaspar, T. C. Droubay, J. McCloy, M. E. Bowden, V. Shutthanandan, S. M. Heald and S. A. Chambers, *Phys. Rev. B*, 2011, **84**, 245325.
49. L. Farrell, E. Norton, C. M. Smith, D. Caffrey, I. V. Shvets and K. Fleischer, *Journal Of Materials Chemistry C*, 2016, **4**, 126.

50. N. Preissler, O. Bierwagen, A. T. Ramu and J. S. Speck, *Phys. Rev. B*, 2013, **88**, 085305.
51. H. Z. A.Liu, Z. Guo, Y. Meng, G. Liu, E. Fortunato, R. Martins, F. Shan, *Adv. Mater.*, 2017, **29**, 1701599.
52. M. Imada, A. Fujimori and Y. Tokura, *Reviews Of Modern Physics*, 1998, **70**, 1039.
53. K. Horiba, A. Chikamatsu, H. Kumigashira, M. Oshima, N. Nakagawa, M. Lippmaa, K. Ono, M. Kawasaki and H. Koinuma, *Phys. Rev. B*, 2005, **71**, 155420.
54. A. Fujimori, A. Ino, J. Matsuno, T. Yoshida, K. Tanaka and T. Mizokawa, *J. Electron. Spectrosc. Relat. Phenom.*, 2002, **124**, 127.
55. E. L. Ratcliff, J. Meyer, K. X. Steirer, A. Garcia, J. J. Berry, D. S. Ginley, D. C. Olson, A. Kahn and N. R. Armstrong, *Chem. Mat.*, 2011, **23**, 4988.
56. A. Klein, *J. Am. Ceram. Soc.*, 2013, **96**, 331.
57. F. M. F. Degroot, M. Grioni, J. C. Fuggle, J. Ghijsen, G. A. Sawatzky and H. Petersen, *Phys. Rev. B*, 1989, **40**, 5715.
58. K. H. L. Zhang, Y. Du, P. V. Sushko, M. E. Bowden, V. Shutthanandan, S. Sallis, L. F. J. Piper and S. A. Chambers, *Phys. Rev. B*, 2015, **91**, 155129.
59. R. L. Z. Hoyer, L. C. Lee, R. C. Kurchin, T. N. Huq, K. H. L. Zhang, M. Sponseller, L. Nienhaus, R. E. Brandt, J. Jean, J. A. Polizzotti, A. Kursumovic, M. G. Bawendi, V. Bulovic, V. Stevanovic, T. Buonassisi and J. L. MacManus-Driscoll, *Adv. Mater.*, 2017, **29**, 1702176.
60. G. A. Sawatzky and J. W. Allen, *Physical Review Letters*, 1984, **53**, 2339.
61. M. Taguchi, M. Matsunami, Y. Ishida, R. Eguchi, A. Chainani, Y. Takata, M. Yabashi, K. Tamasaku, Y. Nishino, T. Ishikawa, Y. Senba, H. Ohashi and S. Shin, *Physical Review Letters*, 2008, **100**, 206401.
62. J. R. Manders, S. W. Tsang, M. J. Hartel, T. H. Lai, S. Chen, C. M. Amb, J. R. Reynolds and F. So, *Adv. Funct. Mater.*, 2013, **23**, 2993.
63. G. Natu, P. Hasin, Z. J. Huang, Z. Q. Ji, M. F. He and Y. Y. Wu, *ACS Appl. Mater. Interfaces*, 2012, **4**, 5922.